Bidirectional tornado modes on the Joint European Torus

P. Sandquist, S. E. Sharapov, M. Lisak, T. Johnson, and JET-EFDA contributors

---

Articles you may be interested in

Understanding the bursty electron cyclotron emission during a sawtooth crash in the HT-7 tokamak
Phys. Plasmas **21**, 012501 (2014); 10.1063/1.4861336

Deuterium beam acceleration with 3rd harmonic ion cyclotron resonance heating in Joint European Torus:
Sawtooth stabilization and Alfvén eigenmodes
Phys. Plasmas **19**, 032115 (2012); 10.1063/1.3696858

Determination of the minimum value of the safety factor from geodesic Alfvén eigenmodes in Joint European
Torus
Phys. Plasmas **17**, 110705 (2010); 10.1063/1.3494212

Studies of burning plasma physics in the Joint European Torus
Phys. Plasmas **11**, 2607 (2004); 10.1063/1.1690763

Mechanism of radial redistribution of energetic trapped ions due to m=2/n=1 kink instability in plasmas with an
internal transport barrier in the Joint European Torus
Phys. Plasmas **10**, 713 (2003); 10.1063/1.1539471

Bidirectional tornado modes on the Joint European Torus

P. Sandquist
EURATOM-VR Association and Department of Radio and Space Science,
Chalmers University of Technology, SE-412 96 Göteborg, Sweden

S. E. Sharapov
EURATOM/UKAEA Fusion Association, Culham Science Centre, Abingdon,
Oxfordshire OX14 3DB, United Kingdom

M. Lisak
EURATOM-VR Association and Department of Radio and Space Science,
Chalmers University of Technology, SE-412 96 Göteborg, Sweden

T. Johnson
EURATOM-VR Association, Fusion Plasma Physics, EES, KTH, 10044 Stockholm, Sweden

JET-EFDA contributors[a]

In discharges on the Joint European Torus [P. H. Rebut and B. E. Keen, Fusion Technol. **11**, 13 (1987)] with safety factor $q(0) < 1$ and high-power ion cyclotron resonance heating (ICRH), monster sawtooth crashes are preceded by frequency sweeping "tornado modes" in the toroidal Alfvén eigenmode frequency range. A suite of equilibrium and spectral magnetohydrodynamical codes is used for explaining the observed evolution of the tornado mode frequency and for identifying temporal evolution of the safety factor inside the $q = 1$ radius just before sawtooth crashes. In some cases, the tornado modes are observed simultaneously with both positive and negative toroidal mode numbers. Hence, a free energy source other than the radial gradient of the energetic ion pressure exciting these modes is sought. The distribution function of the ICRH-accelerated ions is assessed with the SELFO code [J. Hedin *et al.*, Nucl. Fusion **42**, 527 (2002)] and energetic particle drive due to the velocity space anisotropy of ICRH-accelerated ions is considered analytically as the possible source for excitation of bidirectional tornado modes. © *2007 American Institute of Physics*. [DOI: 10.1063/1.2804084]

I. INTRODUCTION

The physics of highly energetic ions in tokamak plasmas is one of the most important burning plasma topics[1] and is investigated on the Joint European Torus (JET). Instabilities of high-frequency waves (50–500 kHz for typical JET parameters) are often excited in JET by resonant interaction between shear Alfvén waves and super-Alfvénic energetic ions accelerated by ion cyclotron resonance heating[2] (ICRH) or by ions produced with neutral beam injection[3] (NBI). Similar excitation of Alfvén instabilities by fusion-born alpha-particles may occur in the burning fusion plasma of ITER, since for typical ITER parameters, the Alfvén speed is just below the velocity of fusion-born alpha particles at birth. Possible interplays between the high-frequency Alfvén instabilities and low-frequency magnetohydrodynamical (MHD) modes, such as sawtooth oscillations in discharges with the central safety factor $q(0) < 1$ (see Refs. 4 and 5) are of major interest for burning plasmas since both Alfvénic and sawtooth instabilities may become strongly coupled through the same population of energetic ions.

When a significant population of energetic ions is accelerated up to the MeV energy range by high-power ICRH in sawtoothing JET discharges, the sawtooth oscillations change their character significantly and become so-called monster sawtooth oscillations.[6] In contrast to sawteeth in Ohmically heated plasmas, the monster sawtooth oscillations have very long periods (~ 1 s or longer), saturating, or even decreasing the central electron temperature, i.e., $dT_e(0)/dt \leq 0$, during the precrash phase, and much shorter crash times (~ 50 μs). Monster sawtooth crashes produce larger drops in electron temperature and trigger neoclassical tearing modes more often. The long period of such sawteeth is attributed to the stabilizing effect of ICRH-accelerated energetic ions,[7] while the short crash time is explained by the electron inertia, which introduces a very short time scale in Ohm's law in a singular layer surrounding the $q = 1$ magnetic flux surface.[8] However, some characteristics of the monster sawtooth behavior, such as the saturation or decrease of electron temperature at the precrash phase, as well as the very occurrence of the crash while the fast ion stabilization persists, were more difficult to explain.

It was suggested that $n = 1$ fishbone oscillations preceding the crashes of monster sawteeth may expel fast ions from inside the $q = 1$ radius, thus triggering loss of fast ion stabilization with subsequent crashes.[7] However, it was then found that not all crashes have precursors in the form of fishbones, and a search for alternative possibilities continued.

In the late 1990s, significant improvements made in the detection of Alfvénic instabilities allowed an identification of another precursor to monster sawtooth crashes—so-called "tornado" modes[9–11] with frequencies much higher than the frequency of the $n=1$ fishbones. Frequencies of these multiple modes are close to the frequency range of toroidal Alfvén eigenmodes (TAEs), but in contrast to the usual TAEs, they exhibit a significant sweep in frequency and are observed with mode numbers decreasing one-by-one during the time preceding the sawtooth crashes. Due to the sweeping frequency evolution, tornado modes were first associated with energetic particle modes (EPMs). It was noted from the very beginning[9] that tornado modes cause a much more significant degradation of the fast ion confinement than TAEs. It was also suggested[10] that the very occurrence of the monster sawtooth crash may be caused by the tornado modes expelling fast ions from the central region of plasma inside the $q=1$ radius, so that the fast ion stabilizing effect decreases below a critical value and the sawtooth crash can no longer be prevented by the fast ions. In accordance with such theory, the saturation or decrease of electron temperature, i.e., $dT_e/dt \leq 0$, at the precrash phase, is not caused by a sudden change in electron heat conductivity. Instead, a saturation or decrease of the electron heating source causes the electron temperature to roll over as the fast ion pressure gradient exceeds the critical value for excitation of tornado modes, and these modes expel fast ions from the center of the plasma to the region outside the $q=1$ magnetic surface.

In parallel, a theory of low-shear TAEs was developed in order to explain modes observed in Tokamak Fusion Test Reactor deuterium-tritium experiments, in which the values of β exceeded the critical threshold for TAE suppression.[12,13] However, it was only understood after observation of odd parity[13] tornado modes on JET that the tornado modes are not EPMs as suggested in Ref. 10, but they are low-shear TAEs inside the $q=1$ radius.[14] The significant frequency sweep of tornado modes and the sequence of toroidal mode numbers are caused by the proximity of the modes to the magnetic axis and by $q(0)$ decreasing in time; both effects were established in ideal MHD modeling with MISHKA and NOVA-K codes.[14]

The identification of tornado modes as low-shear TAEs inside the $q=1$ radius made it possible to model these modes and to develop a dedicated experimental scenario for studying tornadoes in JET plasmas with monster sawteeth.[2] It was noted in Ref. 14 that tornado modes are localized deep in the plasma core and they rarely have more than two coupled poloidal harmonics. Under such conditions, it became clear that detection of tornado modes is a significantly more difficult task than detection of TAEs outside the $q=1$ radius, since TAEs are closer to the magnetic pick-up coils (Mirnov coils) outside the plasma, and TAEs consist of multiple harmonics due to greater magnetic shear outside the $q=1$ radius. The progress in detecting Alfvén eigenmodes with core plasma diagnostics on JET such as interferometry[15–17] and reflectometry[18] made it possible to observe tornado modes even if these were localized very close to the magnetic axis and thus were not seen by Mirnov coils.

Recent JET experiments devoted to tornado modes have revealed that in many cases tornado modes with both positive and negative toroidal mode numbers are observed simultaneously. The spectroscopic analysis resembles the study previously done in Ref. 19, where the sequence of TAE excitation prior to sawtooth crashes, as well as ellipticity-induced Alfvén eigenmode (EAE) excitation following the sawtooth crashes were studied. It is our intention to study the experimentally observed bidirectional EAEs in another paper.

In cylindrical geometry, shear Alfvén waves satisfy the dispersion relation $\omega = |k_{\parallel m}(r) v_A(r)|$, where $k_{\parallel m}(r)$ is the parallel component of the wave vector as a function of minor radius r and $v_A(r) = B_0/\sqrt{4\pi\rho_0}$ is the Alfvén velocity. However, these waves suffer from strong continuum damping. In tokamaks, the toroidal geometry introduces perturbations, known as toroidal coupling terms, which lead to a coupling between neighboring poloidal harmonics of the wave,[20,21] expressed by the coupling condition

$$k_{\parallel m}(r_m) = -k_{\parallel m-1}(r_m). \tag{1}$$

The resulting TAE gap structure supports discrete frequency TAEs at magnetic flux surfaces characterized by

$$q(r_m) = \frac{m-1/2}{n}, \tag{2}$$

where m and n are the poloidal and toroidal mode numbers, respectively, in the Fourier decomposition of the wave. Moreover, the frequency of TAEs within the TAE gap range is given by[22]

$$\omega_{\text{TAE}}^2 \simeq \left(\frac{v_A(r)}{2q(r)R_0}\right)^2 \left(1 \pm \frac{5}{2}\frac{r}{R_0}\right), \tag{3}$$

where R_0 is the major radius of the torus.

TAEs can be modeled with MHD codes in order to verify the experimentally observed bidirectional modes. However, whereas MHD modeling of TAEs gives a deeper understanding of plasma equilibrium properties, mode locations, and mode widths, it does not consider the question of drive necessary for the excitation of the bidirectional tornado modes. The drive coming from a monotonically decreasing pressure is only positive for modes propagating in the ion diamagnetic direction, which corresponds to propagation in the same direction as inductive current (copropagation) on JET. Mathematically, the necessary condition for a positive drive of TAEs due to hot ions is $\omega < \omega_\star$,[21] where the diamagnetic frequency is given by

$$\omega_\star = \frac{nv}{\omega_c R_0}\frac{\partial f_0/\partial J_\varphi}{\partial f_0/\partial v}. \tag{4}$$

Here, f_0 is the unperturbed hot ion velocity distribution function, J_φ is the toroidal canonical momentum, $\omega_c = eB_0/cM$ is the cyclotron frequency, where M is the particle mass and v is the particle velocity. In order to explain counterpropagating tornado modes with $n < 0$, the drive coming from fast ion anisotropy in the velocity space[23] has to be considered. Analytic theory for the drive was previously carried out in Ref. 24, where the stabilizing effects due to the mode structure
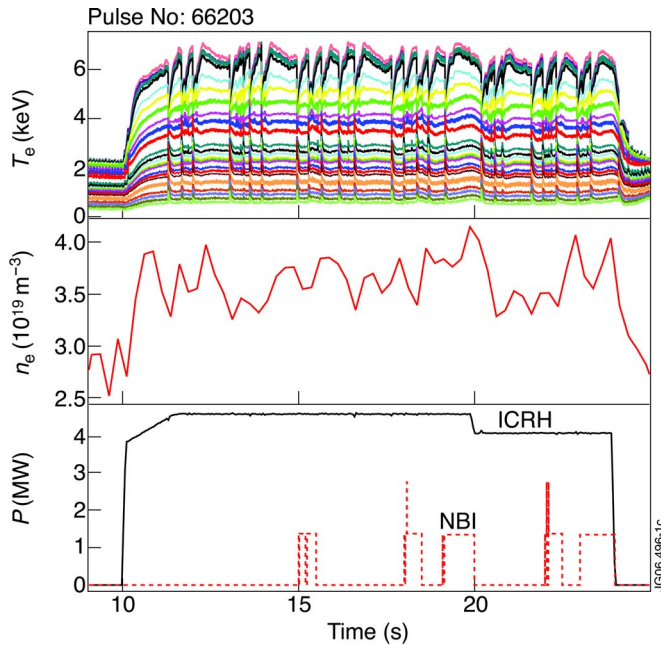
FIG. 1. (Color online) Top: Electron temperature T_e measured with multi-channel ECE diagnostics at different radii on JET. Middle: Electron density $n_e(0)$ measured with LIDAR. Bottom: ICRH (black, solid line) and diagnostic NBI (red, dashed line) power waveforms.

FIG. 2. (Color online) Transition from short-period, $\sim$100 ms, Ohmic sawteeth to long-period, $\sim$1 s, monster sawteeth, is observed after high-power ICRH is applied.

were considered for excitation by both passing and trapped hot ions in a small banana width limit.

The paper is organized as follows. In Sec. II, experimental data for tornado mode discharge No. 66203 of the tornado mode session on JET is presented. The existence of the observed bidirectional tornado modes is then verified, by a suite of MHD codes, in Sec. III. Theory for bidirectional tornado mode drive, arising from velocity anisotropy in the ICRH-accelerated fast ion distribution function, is presented and applied to experimental data in Sec. IV. Finally, we summarize and discuss the results obtained in Sec. V.

II. EXPERIMENTAL OBSERVATIONS ON JET

Figure 1 shows electron temperature, line-average electron density, and power waveforms in JET discharge (pulse No. 66203) with magnetic field 2.7 T and plasma current 2 MA, where bidirectional tornado modes were observed.

High-power ICRH with a frequency corresponding to the hydrogen cyclotron frequency at the magnetic axis was used for accelerating hydrogen minority ($n_H/n_e \approx 2.5\%$) ions, so that ICRH generated an energetic tail of hydrogen ions and, via the second-harmonic resonance, some deuterium tail. Low-power blips of NBI were used for measuring the ion temperature and the safety factor profile. An inductive current flat top of 2 MA was obtained 1 s before the start of ICRH, and short-period sawteeth in the Ohmic phase of the discharge appeared before ICRH power was applied. The transition from Ohmic sawteeth to monster sawteeth is shown in Fig. 2.

In this discharge, at least eight monster sawteeth satisfying $dT_e/dt \leq 0$ prior to the sawtooth crashes were observed as can be seen from T_e measurements in Fig. 1, and all of
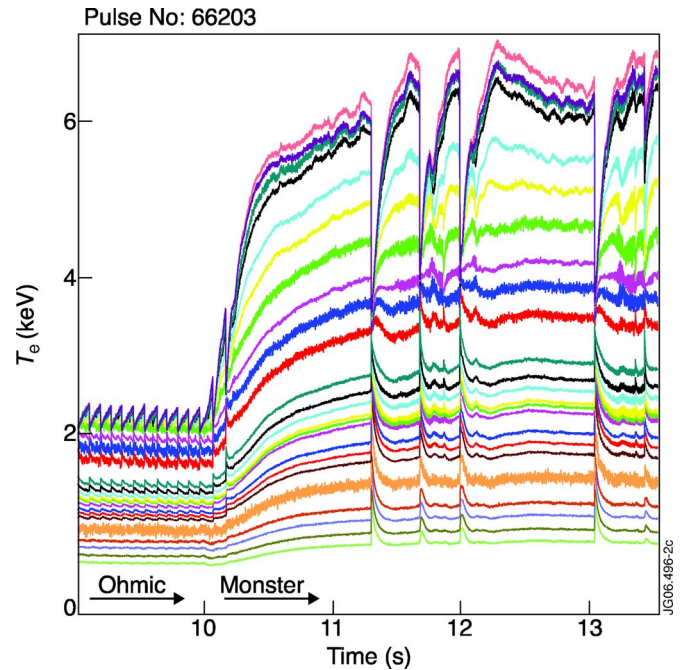
them were preceded by bidirectional tornado modes. Figures 3(a)–3(c) show the examples of bidirectional tornado modes preceding the first monster sawtooth crash at $\sim$11.3 s.

Figure 3(a) shows toroidal mode numbers of the poloidal magnetic field perturbations derived from the phase shifts between signals measured with toroidally separated Mirnov coils located just outside the plasma. The toroidal mode numbers of the cocurrent propagating modes with positive n are seen to decrease in time one-by-one from $n=9$ to $n=2$ as the sawtooth crash approaches. The counterpropagating modes with negative toroidal mode numbers display a less regular sequence of appearance, occurring simultaneously with $n=-6$, -5, and, somewhat later, with $n=-4$ and $n=-2$.

Figures 3(b) and 3(c) show spectrograms of electron density perturbations detected in the same frequency range with the O-mode interferometry.[15] Figures 3(a) and 3(b) show that tornado modes with both positive and negative mode numbers are detected with Mirnov coils and O-mode interferometry. However, the O-mode interferometry also shows a set of sweeping frequency Alfvén cascades in the range 50–150 kHz, which were hardly visible by using the Mirnov coils.

In order to clarify the coexistence of Alfvén cascades and tornado modes, another example of tornado modes preceding sawtooth crash is shown in Fig. 4. Figure 4 shows, somewhat more clearly than in Fig. 3(c), an image of both Alfvén cascades and tornado modes detected with the O-mode interferometry. Although there is a frequency gap 200–220 kHz separating Alfvén cascades and tornado modes, this figure suggests that tornado modes may be related to Alfvén cascades in this case. It is important to note that Alfvén cascades in the low-shear region inside the $q = 1$ radius, in contrast to the advanced tokamak scenarios
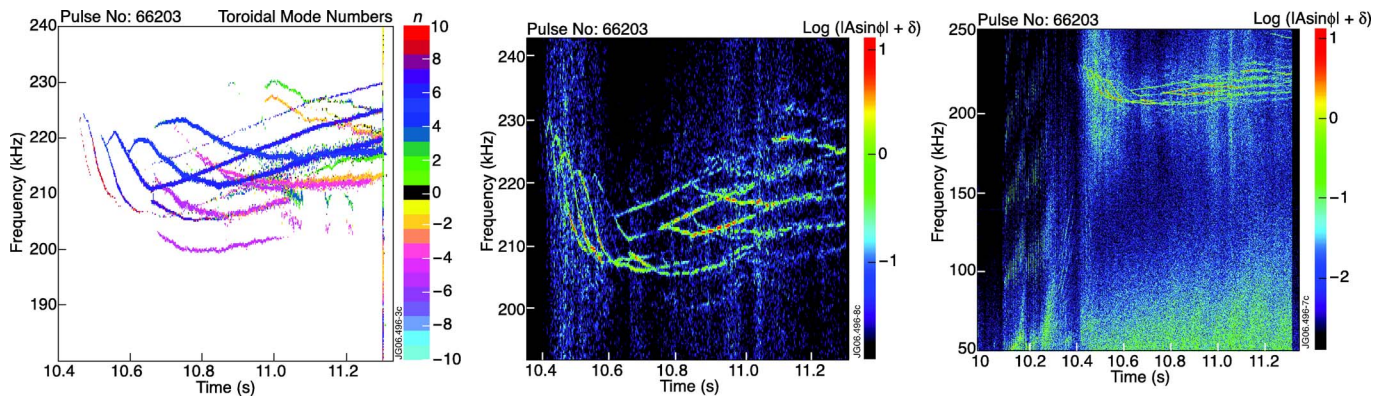
FIG. 3. (Color online) (a) Magnetic spectrogram showing toroidal mode numbers of the observed bidirectional tornado modes preceding the monster sawtooth crash at 11.3 s. (b) Zoom of (c) showing tornado modes with both positive and negative mode numbers in the interferometry data [to be compared to (a)]. (c) Spectrogram of high-frequency density perturbations measured with the O-mode interferometry (frequency 50.47 GHz) (see Ref. 15). Tornado modes are seen in the TAE frequency range around 200–240 kHz; frequency-sweeping Alfvén cascades are seen in the frequency range 50–150 kHz.

with $q > 1$, may not be necessarily associated with a reversed magnetic shear. At least two other effects may play a role in forming the Alfvén cascade eigenmodes very close to the magnetic axis; namely, (i) magnetic axis itself may form a potential barrier in ideal MHD providing a sufficiently flat (but still monotonic) q-profile,[25] and (ii) the finite Larmor radius effects of thermal ions may form Rosenbluth-Rutherford modes in the vicinity of the magnetic axis.[26]

Taking into account that the experimental data shows only one set of Alfvén cascade eigenmodes in Figs. 3(c) and 4, it is unlikely that these modes have negative toroidal mode numbers, which would be shifted in frequency due to the Doppler shift. Since the problem of explaining the bidirectional tornado modes seems to be independent of the relation between tornado modes and Alfvén cascades, we focus here on the bidirectional modes in the TAE-frequency range only

in what follows, while the very interesting question about the coupling of tornado modes and Alfvén cascades will be considered elsewhere.

It is of special interest to consider bidirectional tornado modes in ICRH-heated plasmas during low-power diagnostic NBI. The application of low-power NBI heating does not lead to a strong anisotropy in the velocity distribution function. However, the unbalanced beam injection on JET spins up the plasma toroidally and this toroidal rotation causes Doppler shifts in frequencies of modes with different toroidal mode numbers. In this way, frequencies of positive and negative mode numbers are well separated and it makes the analysis of the data less ambiguous. Figure 5 shows bidirectional tornado modes during NBI as these are observed with Mirnov coils. Figure 6 shows high-frequency density pertur-
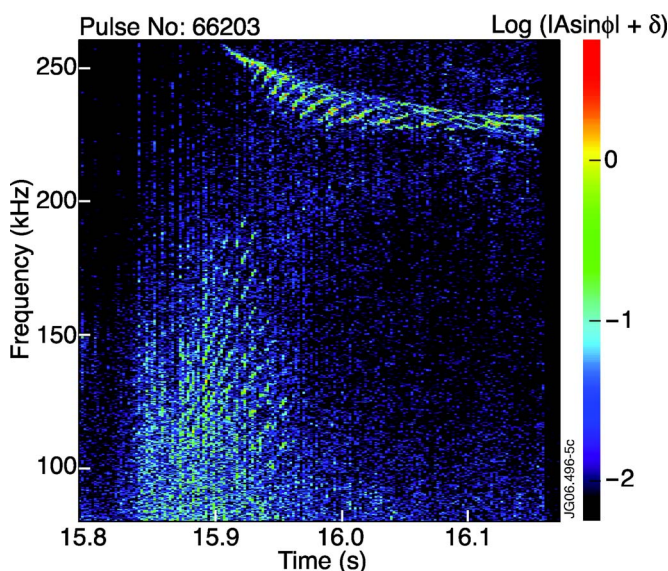

FIG. 4. (Color online) Spectrogram of high-frequency density perturbations measured with the O-mode interferometry (frequency 50.47 GHz). Tornado modes are seen in the TAE frequency range around 200–240 kHz; frequency-sweeping Alfvén cascades are seen in the frequency range 100–200 kHz.
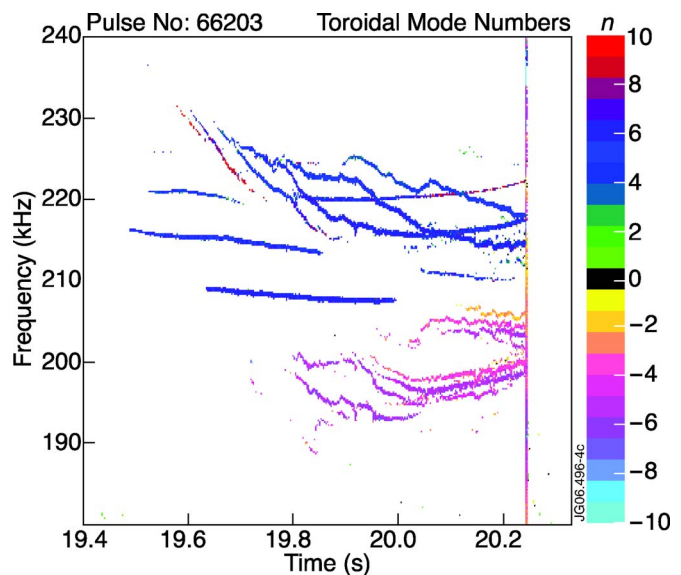

FIG. 5. (Color online) Magnetic spectrogram showing the temporal evolution of tornado modes and TAEs (no chirping) at the time $t=20.2$ s in JET discharge No. 66203. From toroidal mode number analysis, tornado modes with both negative and positive mode numbers are identified. Their existence is verified by modeling (Sec. III) and is further motivated by a velocity anisotropy drive estimate (Sec. IV).
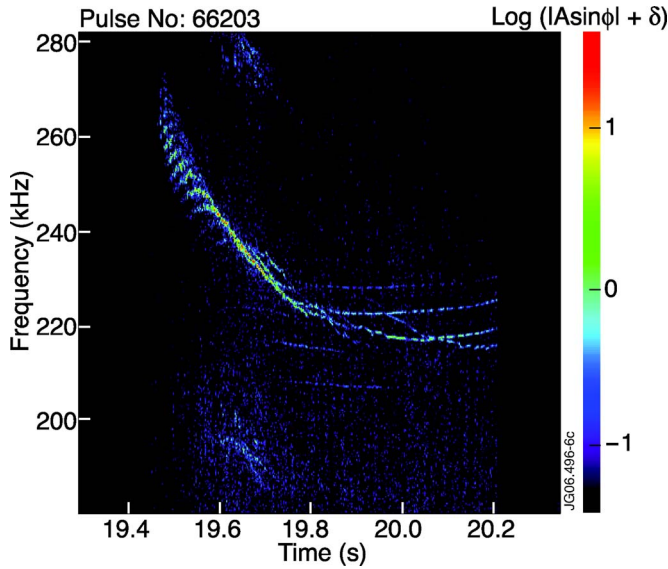
FIG. 6. (Color online) Spectrogram of high-frequency density perturbations measured with the O-mode interferometry (frequency 50.47 GHz). Positive tornado modes are seen in the TAE frequency range around 200–240 kHz. However, the negative tornado modes, measured by Mirnov coils in Fig. 5, are not detected by interferometry.
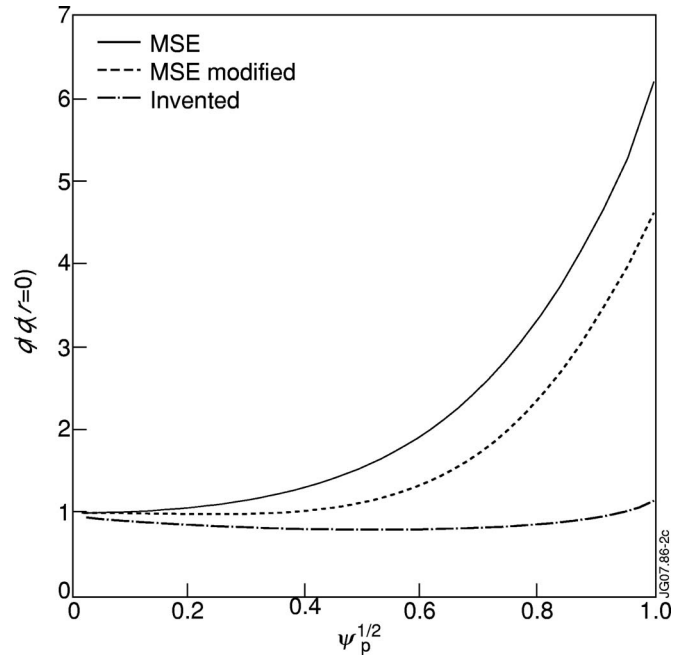
FIG. 7. Radial safety factor profiles $q(r)$ normalized to the value on the magnetic axis, $q_0 = q(r=0)$, as functions of normalized poloidal flux, $\psi_p^{1/2} \sim r/a$, where a is the minor radius of the plasma edge. The three equilibria are the MSE measured equilibrium (solid line), a nonmonotonic modified MSE equilibrium (dashed line), and an equilibrium from JET shot No. 54956 (dash-dotted line). Variations of the two nonmonotonic q-profiles are also modeled.

bations detected with the O-mode interferometry at the same time. No Alfvén cascades are detected by interferometry in this case.

Figure 5 shows the results of a toroidal mode number analysis of JET shot No. 66203 just before a giant sawtooth crash at $t=20.2$ s. The excitation of tornadoes with negative mode numbers ($n<0$) is delayed in comparison to the excitation of positive mode number ($n>0$) tornadoes. Moreover, some of the counterpropagating modes are upward-chirping, whereas copropagating modes are downward-chirping. From the observation of negative mode number tornadoes, our first idea was that we are most likely to have a hollow fast ion pressure profile in these discharges due to low-field side ICRH. However, modeling of the ICRH-accelerated distribution function with the self-consistent code SELFO[27] shows that this is not the case at the time of excitation of tornado modes. Possible explanations of the observation of negative toroidal mode number tornadoes are discussed further in Sec. IV.

We note that at about twice the TAE range of frequencies, bidirectional EAEs are found to be excited after the sawtooth crash, when the safety factor profile has been lifted due to the effect of the reconnection event. Since Alfvén cascades are also observed, as Figs. 3(c) and 4 show, we are in a position to test whether a reversed shear safety factor profile better models the observed temporal evolution of tornado modes in Fig. 5. In Sec. III, this idea is further investigated.

III. MODELING WITH MHD CODES

The experimental observations of bidirectional tornado modes on JET are investigated further below with a suite of MHD codes: HELENA,[28] CSCAS,[29] and MISHKA.[30,31] The aim of the MHD modeling is to identify the radial location of the

tornado modes, to verify the toroidal mode numbers suggested by the mode number analysis, and to reproduce the temporal evolution of the mode frequencies.

A. Equilibrium reconstruction

The MHD code HELENA[28] is first used to construct an equilibrium in straight field line coordinates from a motional Stark effect (MSE) measured safety factor profile. The safety factor is defined through

$$q(r) = \frac{\mathbf{B} \cdot \nabla \zeta}{\mathbf{B} \cdot \nabla \theta} \simeq \frac{r B_\zeta}{R_0 B_\theta}, \tag{5}$$

where θ and ζ are the poloidal and toroidal coordinates, respectively, and B_ζ and B_θ are the toroidal and poloidal magnetic field components, respectively. Since $B_\theta/B_\zeta \sim \mathcal{O}(\epsilon)$, Eq. (5) states that $q \sim \mathcal{O}(1)$.

In order to study the possibility of a reversed magnetic shear scenario, a reversed shear equilibrium just outside the error bars of MSE diagnostics as well as a reversed shear equilibrium from a similar type of discharge, but with larger negative magnetic shear, have been generated. The safety factor profiles of the three basic equilibria used for tornado mode modeling are illustrated in Fig. 7.

B. Alfvén eigenmode modeling

The Alfvén continuum gap (ACG) structure, which is generated with the CSCAS code[29] and is modified as the value of the safety factor changes, provides a graphical way to determine the radial positions and normalized frequency
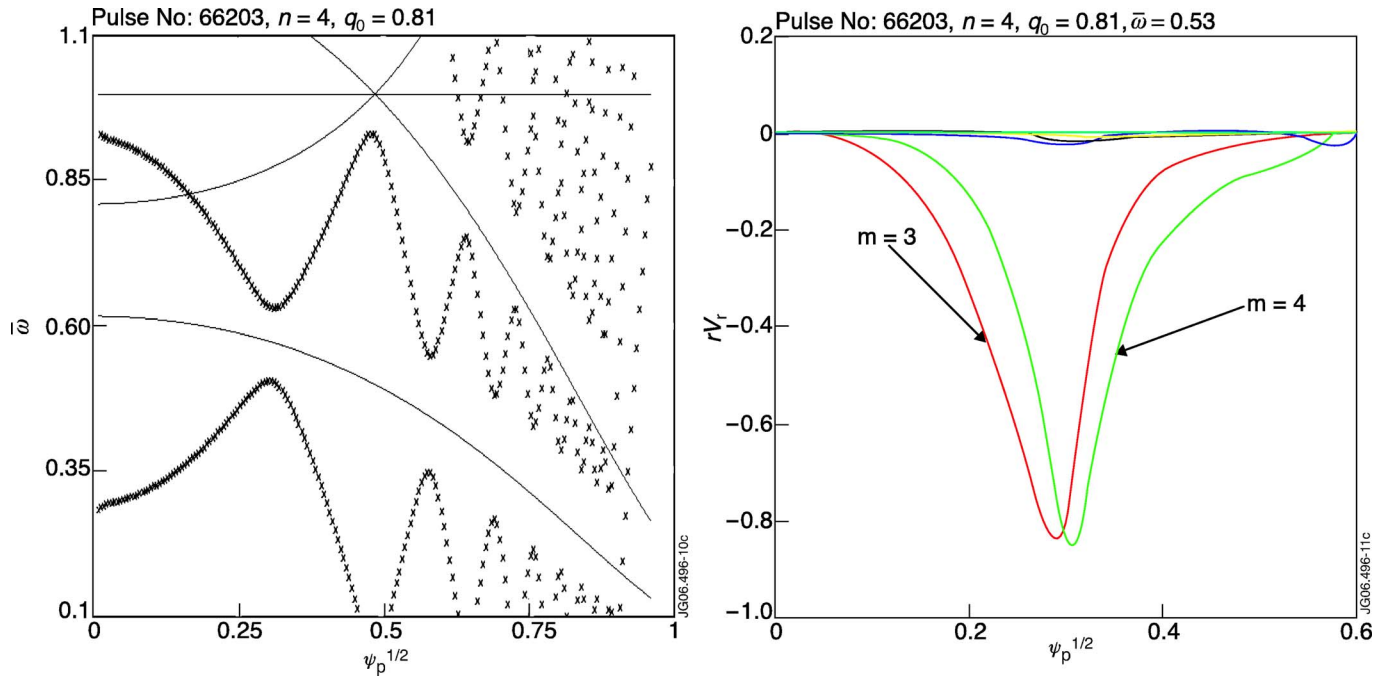
FIG. 8. (Color online) Left: Alfvén continuum gap structure (from CSCAS) for $n=+4$ shear Alfvén waves with a safety factor on magnetic axis $q_0=0.81$. Thin lines denote $q(\psi_p^{1/2})$ and $n_e(\psi_p^{1/2})=$const profiles and the central frequencies of TAE and EAE gaps. Right: Mode structure (from MISHKA) of the mode associated with the gap at $\psi_p^{1/2}=0.31$.

range of possible TAEs. In particular, since the safety factor profile is included in the ACG structure diagram, it is instructive to consider the CSCAS output in order to judge whether TAEs are to be located outside the $q=1$ surface, or inside the $q=1$ surface, in which case they are called tornado modes.

Starting from the reconstructed MSE equilibrium, a sweep in the safety factor value on the magnetic axis is performed with the HELENA code. For each value of $q(r=0)=q_0$, the MHD spectral code MISHKA[30,31] is used in order to scan the Alfvén continuum gap structure, observed in CSCAS for tornado modes. An initial guess of the normalized eigenmode frequency,

$$\bar{\omega} = \frac{\omega R_0}{v_A}, \qquad (6)$$

is then made. Note that the center of the TAE gap corresponds to normalized frequency $\bar{\omega}=1/2$ [see Eq. (3)]. A complete scan of the TAE gap in this way finds all the supported modes by the specific $q_0=$const equilibrium.

The supported modes consist of two dominant poloidal harmonics, for which the poloidal mode number m is consistent with the coupling condition [Eq. (1)]. Representative tornado mode structures for $n=+4$, $+5$, and $+6$ are illustrated, together with the ACG structure from CSCAS, in Figs. 8–10.

As the modeled TAEs inside $q=1$ are shifted radially outwards, due to a decrease in q_0, they start to couple to edge-localized modes. In order to minimize this coupling, it is appropriate to consider a smaller number of grid points, which decreases the amplitude of singular edge-localized

continuum modes so that the bulk of TAE modes becomes more visible, and to introduce a perfectly conducting wall in MISHKA.[32]

C. Modeling results

In order to describe the results of bidirectional tornado mode modeling, we assume (i) a linear decrease of q in time, and (ii) the radial gradient of $q(r)$ from MSE measurements is constant at all times. This facilitates a linear mapping of the modeled decrease in q_0 to the temporal evolution of the normalized tornado mode frequencies. Furthermore, we map the normalized frequency $\bar{\omega}$ by taking the values $v_A(r=0)=7.9\times10^6$ m/s and $R_0=3.0$ m, and including the experimentally observed Doppler shifts. The validity of considering only constant values for the Alfvén velocity is confirmed by light detection and ranging (LIDAR) Thompson scattering measurements of electron density. The plasma rotation frequency is measured by charge exchange, and the measured frequency in the laboratory frame is given by

$$f_{lab} = f_{TAE} + n f_{rot}, \qquad (7)$$

where $\omega_{TAE}=2\pi f_{TAE}$ is the TAE frequency in the rest frame [Eq. (3)], and $f_{rot}(r=0.4)=2.3$ kHz at $t=20$ s in our discharge, JET shot No. 66203. The results of the MSE equilibrium modeling are presented in Fig. 11, from which a good agreement with the experimental data in Fig. 5 is confirmed.

From Figs. 3(c) and 4, we learn that evidence for a reversed shear scenario exists. Therefore, we proceed with two reversed shear safety factor equilibria; the one constructed from the MSE measured equilibrium (just outside MSE error
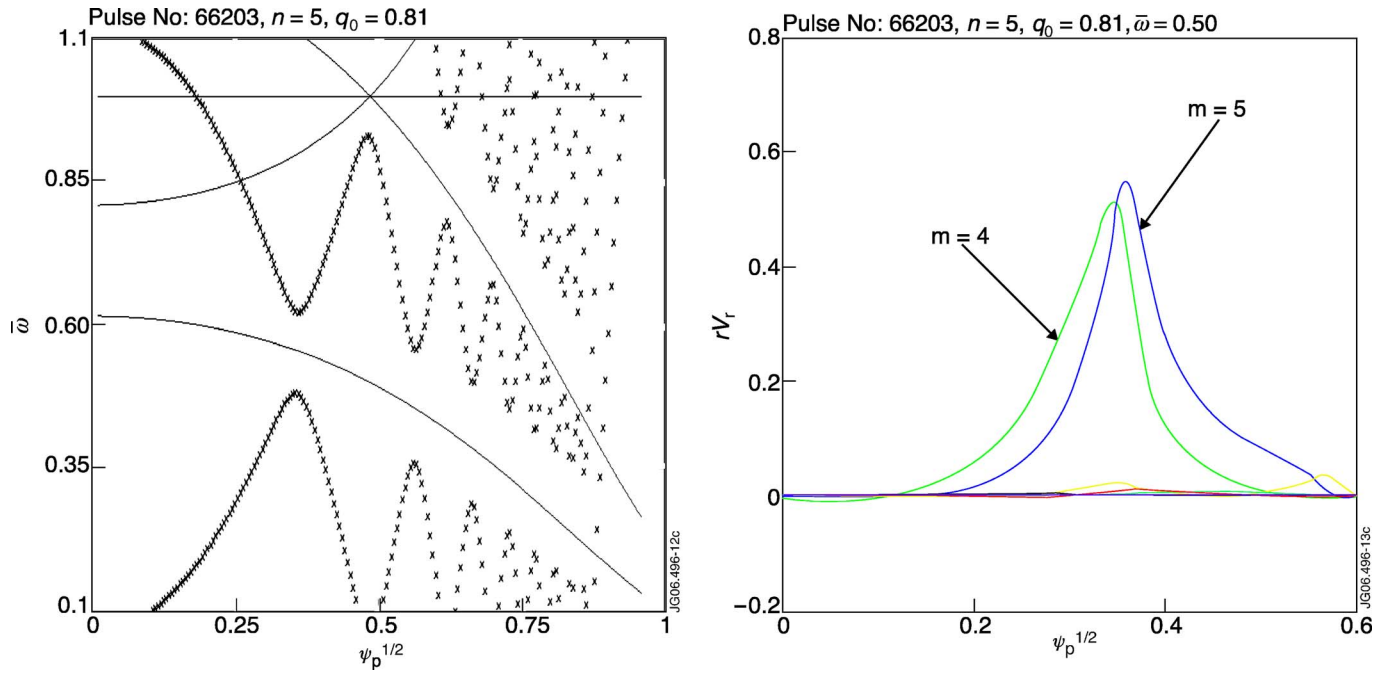
FIG. 9. (Color online) Left: Alfvén continuum gap structure (from CSCAS) for $n=+5$ shear Alfvén waves with a safety factor on magnetic axis $q_0=0.81$. Thin lines denote $q(\psi_p^{1/2})$ and $n_e(\psi_p^{1/2})=$const profiles and the central frequencies of TAE and EAE gaps. Right: Mode structure (from MISHKA) of the mode associated with the gap at $\psi_p^{1/2}=0.36$.

bars) and the one that uses a strongly reversed safety factor from JET shot No. 54956. These two additional safety factor profiles are depicted in Fig. 7. The proposed idea consists of identifying (i) $\hat{s}>0$ positive tornadoes, where $\hat{s}=(r/q)\mathrm{d}q/\mathrm{d}r$ is the magnetic shear of the safety factor profile, (ii) $\hat{s}>0$ negative tornadoes associated with the same magnetic surface, and (iii) $\hat{s}<0$ negative tornadoes, which

appear late before the sawtooth crash and are associated with a magnetic surface with a value of q one step lower than the previous one [see Eq. (2)]. The third group of tornado modes would then complete the "corridor" of tornado modes located at two different radii and expel resonant hot ions, potentially giving rise to the sawtooth crash.

Apart from being able to handle three groups of tornado
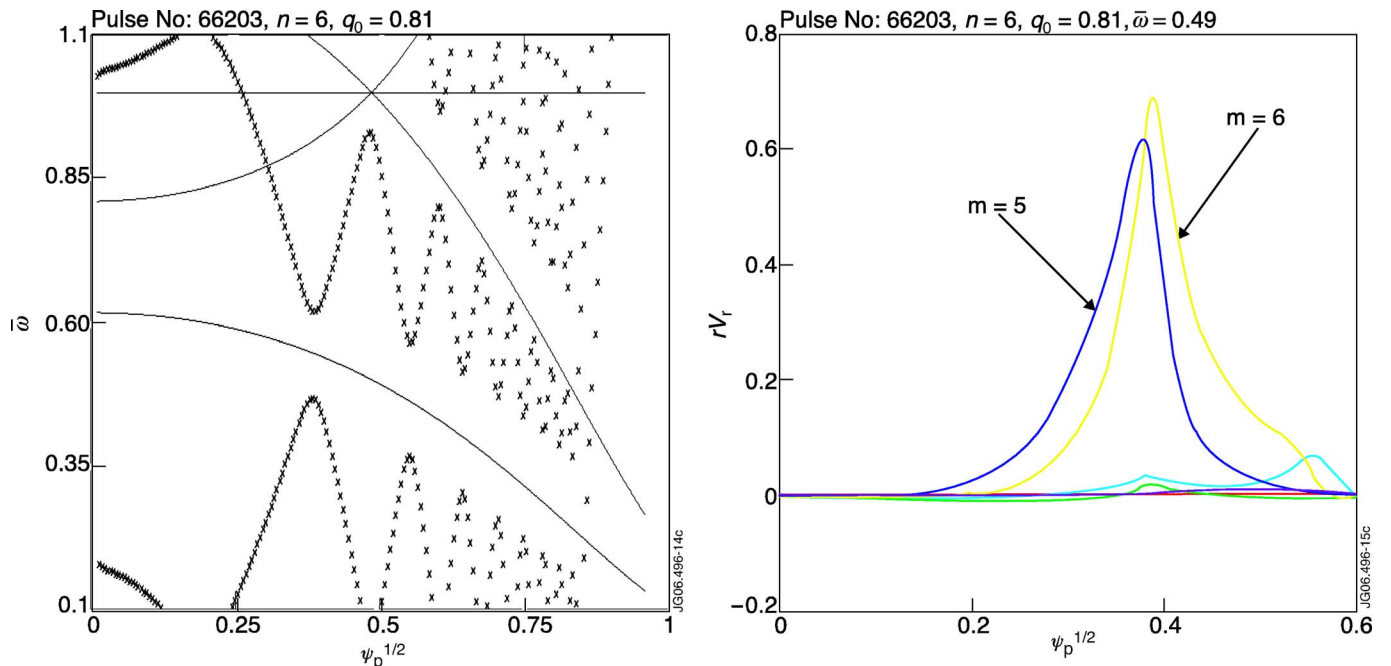

FIG. 10. (Color online) Left: Alfvén continuum gap structure (from CSCAS) for $n=+6$ shear Alfvén waves with a safety factor on magnetic axis $q_0=0.81$. Thin lines denote $q(\psi_p^{1/2})$ and $n_e(\psi_p^{1/2})=$const profiles and the central frequencies of TAE and EAE gaps. Right: Mode structure (from MISHKA) of the mode associated with the gap at $\psi_p^{1/2}=0.39$.
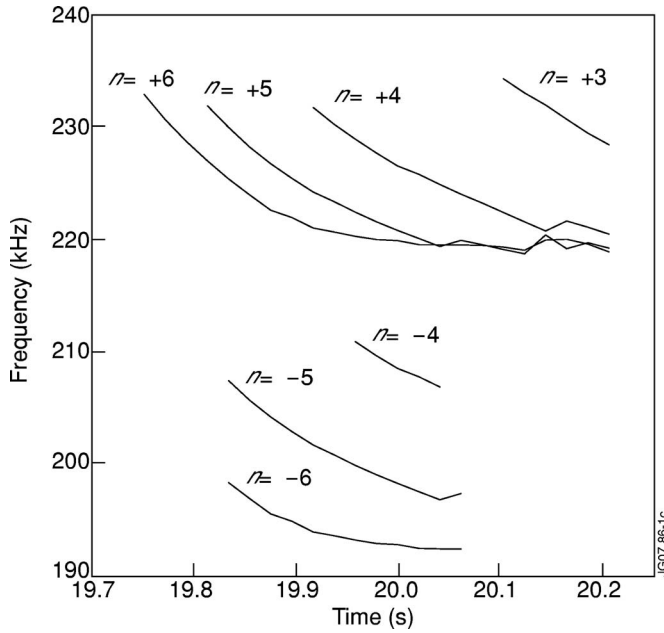
FIG. 11. Spectrogram showing the temporal evolution of modeled tornado modes before the sawtooth crash event at $t_{crash}=20.2$ s in JET discharge No. 66203. The agreement with experimental data is verified by a comparison with Fig. 5. However, the experimental observation of two groups of multiple counterpropagating tornado modes for $t \gtrsim 20.1$ s is not reproduced, as discussed in the text.

modes, the reversed shear scenario would be able to give rise to a group of multiple low-shear TAEs (LSTAEs). For a low enough shear, the number of LSTAEs is given by the scaling formula[33]

$$N_{LSTAE} \sim \epsilon/\hat{s}. \tag{8}$$

The minimum of the reversed shear safety factor profile (q_{min}) for this profile is then artificially moved radially inwards in order to obtain two to three LSTAEs. We modify the polynomial coefficients of the expression for the amplitude of the two flux functions in the Shafranov equation, from which the HELENA equilibrium is obtained. The two to three LSTAEs found in this way have the correct frequency chirping and frequency spacing in order to explain the lower group of $n<0$ tornadoes.

However, the difference in frequencies between the upper and lower groups of counterpropagating tornado modes is found to be too high—a factor of $q(r_6)/q(r_5)|_{n=6}$ $=0.917/0.75$—due to different resonant flux surfaces [see Eq. (2)]. This would actually make the upper group of counterpropagating modes higher in frequency than the copropagating modes, in contradiction to what is experimentally observed and illustrated in Fig. 5. The idea of having a reversed shear equilibrium is therefore abandoned.

Returning to the modeling of the MSE measured safety factor profile equilibrium, we explain the change in spectral behavior of the tornado modes, both positive and negative, around $t=20$ s, by a formation of global TAEs. A similar transition, from local to global Alfvén eigenmodes, was reported in Ref. 32. The reason for the transition to global structure comes from an increase of the shear $\hat{s}$ as the mode moves radially outwards, locked at a position determined by

Eq. (2). After the modes have transformed into a global structure, their spectroscopic use for determining the safety factor $q(r)$ is lost.[32]

We note that our modeling results are in agreement with the copropagating tornado modes and the lower counterpropagating tornado modes, but an explanation of the multiplicity of the two groups of counterpropagating modes for $t \simeq 20.1$ s, i.e., just before the sawtooth crash, also seen in Fig. 5, has to be sought. These additional counterpropagating tornado modes are not seen in any other of the six sawtooth crashes in JET discharge No. 66203, so perhaps it is not statistically justified to give an account of these tornado modes.

IV. TAE GROWTH RATE THEORY

Several theoretical models have predicted the presence of TAE instability due to the resonant interaction with hot ions (cf. Refs. 21 and 34), where it has been shown that the TAEs can be strongly excited if the mode frequency ω is lower than the diamagnetic frequency of the fast ions ($\omega_\star$). In Ref. 24, a generalized expression for the linear growth rate of the TAEs, which takes into account the large particle orbit width effects and the effect of mode localization as well as the excitation by both passing and trapped hot ions, is derived. An application of this theory to a strongly anisotropic slowing-down velocity distribution generated by NBI and of fusion produced alpha particles has shown that stabilization of the TAE instability due to large particle orbit width is much more pronounced in the case of an isotropic alpha particle velocity distribution. Here, we analyze the general expression for the TAE instability growth rate with respect to the role of the anisotropy in the hot particle velocity distribution.

According to Refs. 35 and 24, the destabilization of TAEs is sensitive to the ratio between the radial excursion of the hot particle orbits from the flux surfaces (Δ_b) and the TAE localization scale length (Δ_m). In the limit of low magnetic shear and large mode numbers, the inner and outer mode structure of the TAE can be described by[22]

$$\Phi_m^{(i)} = C_m \left[\frac{1}{\alpha_m} \arctan\left(\frac{r-r_m}{\Delta_m^{(i)}}\right) + \frac{1}{2} \ln \left| \left(\frac{r-r_m}{\Delta_m^{(i)}}\right)^2 + 1 \right| \right] + const, \tag{9}$$

$$\Phi_m^{(o)} = -C_m K_0 \left(\left| \frac{r-r_m}{\Delta_m^{(o)}} \right| \right), \tag{10}$$

where $K_0(x)$ is the zeroth-order MacDonald function, α_m $=4/(\pi\hat{s})$, $\hat{s}$ is the magnetic shear, r_m is the mode localization radius, R_0 is the major radius at the magnetic axis, $\Delta_m^{(i)}$ $=(\pi/8)dr_m^2/R_0$ with $d=2.5-5$ and $\Delta_m^{(o)}=r_m/m$ are the inner and outer widths of the mode, respectively, and C_m is a constant determined by the boundary conditions at the gap surface. Note that, in spite of the fact that $\Delta_m^{(i)}/\Delta_m^{(o)}$ $=r_m/R_0 \ll 1$, most of the mode energy is concentrated in the inner region of the mode. For well-passing particles, it can be estimated that $\Delta_b^p \simeq qv/\omega_c$, where ω_c is the particle

cyclotron frequency, which for $\omega_\star/\omega$ gives $\Delta_b^p/\Delta_m^{(i)}>1$. For trapped particles, the width of the banana orbits is $(\Delta_b^t)_{max} \simeq 2\sqrt{2}q_m\kappa_{max}v/(\omega_c\epsilon_m^{1/2})$, where $\epsilon_m=r_m/R_0$, implying that $\Delta_b^t/\Delta_m^{(i)}>1$ can be satisfied. Furthermore, the excursion of particle orbits can be comparable to or larger than the orbit

of the excited TAE mode, i.e., $\Delta_b\geq\Delta_m^{(o)}$ if $qv_A/\omega_c\geq r_m/m$ for passing particles and $qv_A/\omega_c\geq\sqrt{\epsilon_m}r_m/m$ for trapped particles, where $v_A=B_0/\sqrt{4\pi\rho_0}$ is the Alfvén velocity.

The general expression for the TAE instability growth rate is given by[24]

$$\gamma=\frac{4\pi^3e_i^2}{c^2\omega_rM^2}\frac{\Sigma_{s,m,\sigma}\int dJ_\varphi\int E dE\int(1/\omega_b)d\lambda\,\delta(\omega_r+m\langle\dot\theta\rangle-n\langle\dot\varphi\rangle-s\omega_b)|G_m|^2\hat\Pi f_0}{\Sigma_m\int drr(|\tilde\Phi_m'|^2+(m^2/r^2)|\tilde\Phi_m|^2)v_A^{-2}},\tag{11}$$

where

$$G_m=\int_0^{\tau_b}\frac{dt}{\tau_b}v_D\left[\tilde\Phi_m'\sin\theta-\frac{im}{r}\tilde\Phi_m\left(\cos\theta-i\frac{v_\perp}{v_D}\frac{d}{d\xi}\right)\right]$$
$$\times J_0(\xi)e^{-iS_0(0,t)}\tag{12}$$

and

$$\hat\Pi=\omega_r\frac{\partial}{\partial E}-\frac{n}{M\omega_cR_0}\frac{\partial}{\partial J_\varphi}.\tag{13}$$

Here, $\langle\bullet\rangle=\int(1/\tau_b)\cdot dt$ denotes bounce averaging, ω_r is the real part of the mode frequency, $\omega_b=2\pi/\tau_b$ is the bounce frequency, s is the bounce harmonic number, e_i and M are the ion charge and the ion mass, respectively, f_0 is the unperturbed part of the hot ion velocity distribution function, $E=Mv^2/2$ is the particle energy, $\lambda=\mu B_0/E$ is the pitch-angle variable, with $\mu=Mv_\perp^2/2B_0$ being the magnetic moment, and $J_\varphi=\Psi-hv_\parallel/\omega_c$ is the toroidal canonical angular momentum, where the poloidal flux function is defined as $\Psi=\Psi_p/R_0B_0=\int RB_\theta dr/R_0B_0$, $h=1+(r/R_0)\cos\theta=1+\epsilon\cos\theta$, and $v_\parallel=\mathbf{v}\cdot\mathbf{B}_0/B_0$. Furthermore, $v_D=(v_\parallel^2+v_\perp^2/2)/R_0\omega_c$ is the magnetic drift velocity, $\xi=k_\theta v_\perp/\omega_c$ is the Larmor radius parameter, $J_0(\xi)$ is the Bessel function of the first kind of zeroth order, and

$$S_0(0,t)=\int_0^t dt'(\omega_r+m\dot\theta-n\dot\varphi).\tag{14}$$

The wave field perturbation $\tilde\Phi$ is described by a Fourier decomposition in poloidal harmonics according to

$$\tilde\Phi=\sum_m\tilde\Phi_m(r)e^{-im\theta+in\varphi-i\omega t},\tag{15}$$

where θ and φ are the poloidal and toroidal angles, respectively, and n is the toroidal number. The resonance condition, expressed by the delta function in Eq. (11), is discussed below. The summation over the sign of the particle parallel velocity σ is included in order to incorporate trapped particles, for which $dt\sim\sigma d\theta$ and the trapped particle orbit is divided into two parts: $\sigma=+1$ for $t\in[0,\tau_b/2]$ and $\sigma=-1$ for $t\in[\tau_b/2,\tau_b]$.

In order to analyze the role of anisotropy in the hot ion velocity distribution on the instability growth rate, we follow Ref. 23 and write the operator $\hat\Pi$ in Eq. (13) as

$$\hat\Pi=\omega_r\frac{\partial}{\partial E}-\omega_r\frac{\lambda}{E}\frac{\partial}{\partial\lambda}-\frac{n}{M\omega_cR_0}\frac{\partial}{\partial J_\varphi}.\tag{16}$$

Thus, the sign of the growth rate γ as defined by Eq. (11) is determined by the sign of the expression

$$\frac{\hat\Pi f_0}{\omega_r}=\left(1-\frac{\omega_\star}{\omega_r}\right)\frac{\partial f_0}{\partial E}-\frac{\lambda}{E}\frac{\partial f_0}{\partial\lambda},\tag{17}$$

where the diamagnetic drift frequency is given by

$$\omega_\star=\frac{n}{M\omega_cR_0}\frac{\partial f_0/\partial J_\varphi}{\partial f_0/\partial E}.\tag{18}$$

In the absence of particle anisotropy, i.e., when $\partial f_0/\partial\lambda=0$, and for a Maxwellian particle velocity distribution, i.e., when $\partial f_0/\partial E<0$, Eq. (17) implies a positive growth rate only for copropagating modes $(n>0)$ such that the diamagnetic drift frequency satisfies $\omega_\star>\omega_r$. However, anisotropy may facilitate excitation of copropagating modes whenever $\omega_\star<\omega_r$ as well as excitation of counterpropagating modes having $n<0$. The conditions for this to occur are

$$\partial f_0/\partial\lambda<0,\tag{19}$$

$$|\partial f_0/\partial\lambda|>\frac{E}{\lambda}\left|\frac{\partial f_0}{\partial E}\left(1-\frac{\omega_\star}{\omega_r}\right)\right|,\tag{20}$$

where it is still assumed that $\partial f_0/\partial E<0$.

A. TAE drive due to passing particles

In order to perform the integration along the particle orbits when calculating the growth rate explicitly, we use the equations for particle drift motion,

$$\dot r=-v_D\sin\theta,\tag{21}$$

$$\dot\theta=\frac{v_\parallel}{qR_0}-\frac{v_D}{r}\cos\theta,\tag{22}$$

$$\dot{\varphi} = \frac{v_\parallel}{R_0}. \tag{23}$$

The resonance condition is determined by the delta function in Eq. (11) together with Eqs. (21)–(23). For well-passing particles it becomes

$$\omega_r - k_{\parallel m} v_\parallel - s\omega_b^p = 0, \tag{24}$$

where $k_{\parallel m} = (nq-m)/qR_0$, $\omega_b^p \simeq |v_\parallel|/qR_0$ is the bounce frequency and the superscript p denotes passing particle quantities. By taking $s = \pm 1$, one finds that this resonance condition supports symmetric excitation resonances, $|v_\parallel| = (v_A/3, v_A)$, and passing particles can thus support counter-propagating modes.

1. Local theory: $\Delta_b^p \ll \Delta_m^{(i)}$

For well-passing particles, we find from Eqs. (21)–(23) $\Delta_b^p = v_D/\omega_c$. In the limit $\Delta_b^p \ll \Delta_m^{(i)}$, the function G_m is mainly determined by the inner mode structure. Using the fact that $|\tilde{\Phi}_m^{(i)'}(r_0)/\tilde{\Phi}_m^{(i)}(r_0)| \sim 1/\Delta_m^{(i)} \gg 1/\Delta_m^{(o)} \sim (r_0/m)^{-1}$, one obtains

$$|G_m|^2 \simeq \frac{v_D^2}{4}|\tilde{\Phi}_m^{(i)'}|^2 J_0^2\left(\frac{mv_\perp}{r_m\omega_c}\right)(\delta_{s,1} + \delta_{s,-1}). \tag{25}$$

Substituting Eq. (25) into Eq. (11) we obtain the following expression for the growth rate:

$$\frac{\gamma}{\omega_r} = \frac{4\pi^3 q^2 M^2}{B_0^2} \sum_{v_r = v_A, v_A/3} \int_0^{v_r/\sqrt{2\epsilon}} v_\perp dv_\perp J_0^2\left(\frac{mv_\perp}{r_m\omega_c}\right)$$
$$\times v_r\left(v_r^2 + \frac{v_\perp^2}{2}\right)^2\left[\left(1 - \frac{\omega_\star}{\omega_r}\right)\frac{\partial f_0}{\partial E} - \frac{\lambda}{E}\frac{\partial f_0}{\partial \lambda}\right], \tag{26}$$

where $v_\parallel = v_r$, $J_\varphi = \Psi_m$, and $\omega_r = v_A/2qR_0$. The summation over v_r in the above expression corresponds to the possible resonances $|v_\parallel| = v_A$ and $|v_\parallel| = v_A/3$, and all quantities are calculated at $r = r_m$.

2. Nonlocal theory: $\Delta_m^{(i)} \ll \Delta_b^p \ll \Delta_m^{(o)}$

In this case, the function G_m is still determined by the radial derivative of the inner mode structure, i.e.,

$$G_m = (-1)^s \frac{v_D}{2\pi} \int_0^{2\pi} d\theta \tilde{\Phi}_m^{(i)'}(r_0 + \Delta_b^p \cos\theta)\sin\theta e^{-is\theta}, \tag{27}$$

which to the lowest order in ϵ_m leads to

$$\int_{J_{\varphi 1}}^{J_{\varphi 2}} dJ_\varphi |G_m|^2\left[\left(\frac{\omega_r}{\omega_\star} - 1\right)\frac{\partial f_0}{\partial J_\varphi} - \frac{\lambda}{E}\frac{\partial f_0}{\partial \lambda}\right]$$
$$\simeq \frac{C_m^2}{\Delta_m^{(i)}}\left\{\frac{2v_D^2\epsilon_m}{\pi^2 q}I(D^p)\left[\left(\frac{\omega_r}{\omega_\star} - 1\right)\frac{\partial f_0}{\partial J_\varphi} - \frac{\lambda}{E}\frac{\partial f_0}{\partial \lambda}\right]\right\}\Bigg|_{J_\varphi = \Psi_m}, \tag{28}$$

where $J_{\varphi 1,2} = \Psi_m - (v/\omega_c)[1-\lambda\mp(2-\lambda)\epsilon_m]^{1/2}$, $\Psi_m \simeq r_m^2/2qR_0$, and we have used Eq. (9) to obtain

$$\tilde{\Phi}_m^{(i)'} = C_m\frac{(r-r_m) + \Delta_m^{(i)}/\alpha_m}{(r-r_m)^2 + (\Delta_m^{(i)})^2}. \tag{29}$$

Furthermore,

$$I(D^p) = \int_{-D^p}^{D^p} dy\left|\int_0^\pi d\theta\frac{(y + D^p\cos\theta) + 1/\alpha_m}{(y + D^p\cos\theta)^2 + 1}\sin^2\theta\right|^2 \tag{30}$$

and $D^p = \Delta_b^p/\Delta_m^{(i)}$ with $\Delta_b^p \ll |r_m|$. Substituting Eq. (28) into Eq. (11) together with

$$\int_{r_m-\Delta_b^p}^{r_m+\Delta_b^p} dr|\tilde{\Phi}_m^{(i)'}|^2 \simeq C_m^2\frac{\pi r_m}{2\Delta_m^{(i)}} \tag{31}$$

and taking into account the fact that $I(D^p) \sim 2\pi^2/3D^p$ for $D^p \gg 1$, we find

$$\frac{\gamma}{\omega_r} = \frac{64q^2 M^2}{3B_0^2} \sum_{v_r = v_A, v_A/3} \int_0^{v_r/\sqrt{2\epsilon}} v_\perp dv_\perp I(D^p)$$
$$\times J_0^2\left(\frac{mv_\perp}{r_m\omega_c}\right)v_r\left(v_r^2 + \frac{v_\perp^2}{2}\right)^2\left[\left(1 - \frac{\omega_\star}{\omega_r}\right)\frac{\partial f_0}{\partial E} - \frac{\lambda}{E}\frac{\partial f_0}{\partial \lambda}\right]. \tag{32}$$

3. Nonlocal theory: $\Delta_m^{(o)} \le \Delta_b^p < r_m$

As long as the particle orbit excursion from the magnetic surface Δ_b^p exceeds the outer mode width $\Delta_m^{(o)}$, the function G_m is determined mainly by the outer mode structure. Using the resonance condition (24) and changing the variables according to $r = r_0 + \Delta_b^p \cos\theta$ and $\theta = \omega_b^p t$, we obtain

$$G_m = -i\frac{s\omega_b}{2\pi}\int_0^{2\pi} d\theta\tilde{\Phi}_m^{(o)}(r_0 + \Delta_b^p \cos\theta)J_0^2\left(\frac{mv_\perp}{r_m\omega_c}\right)e^{-is\theta}e^{iW^p\sin\theta} \tag{33}$$

with $W^p = \Delta_b^p/\Delta_m^{(o)}$. Since the mode energy is still mostly determined by the inner mode structure, we substitute Eqs. (31) and (33) into Eq. (11) and obtain

$$\frac{\gamma}{\omega_r} = \frac{32q^2 M^2}{B_0^2} \sum_{v_r = v_A, v_A/3} \int_0^{v_r/\sqrt{2\epsilon}} v_\perp dv_\perp \frac{\Delta_m^{(i)}}{\Delta_b^p}J_0^2\left(\frac{mv_\perp}{r_m\omega_c}\right)$$
$$\times v_r\left(v_r^2 + \frac{v_\perp^2}{2}\right)^2\frac{H(W^p)}{W^p}\left[\left(1 - \frac{\omega_\star}{\omega_r}\right)\frac{\partial f_0}{\partial E} - \frac{\lambda}{E}\frac{\partial f_0}{\partial \lambda}\right], \tag{34}$$

where

$$H(W^p) = \int_{-W^p}^{W^p} dy\left|\int_0^\pi d\theta K_0(|y + W^p\cos\theta|)\right.$$
$$\left.\times\cos(-\theta + W^p\sin\theta)\right|^2. \tag{35}$$

B. TAE drive due to trapped particles

We consider here well-trapped particles with the trapping parameter $\kappa^2 \equiv (1-\lambda+\lambda\epsilon)/(2\epsilon\lambda) \ll 1$ and assume narrow banana orbits, i.e., $|qv_\parallel/(\epsilon r\omega_c)| \ll 1$, the validity of which was confirmed with the use of the CASTOR-K code[36] for tornado modes with $n > 4$. With these assumptions and making use of the equations of particle drift motion (21)–(23), we find that

$$S_0(0,t) \simeq qR_0 k_\parallel (\theta - \theta_1) + (\omega - \omega_D^t)t \tag{36}$$

with $\theta_1 = -2 \arcsin \kappa$ and the relation between time and the poloidal angle defined by $\omega_b^t t = \sigma\{\pi/2 + \arcsin[1/\kappa \sin(\theta/2)]\}$. Here, $\omega_b^t \simeq \sqrt{(\epsilon/2)}(v/qR_0)$ is the bounce frequency and the precessional drift frequency is given by $\omega_D^t \simeq nqv^2/2rR_0\omega_c$. The resonance condition becomes

$$\omega_r - \omega_D^t - s\omega_b^t = 0, \tag{37}$$

which determines the resonant velocities as

$$v_r = v_r^{\pm} = -s \frac{r\omega_c \sqrt{\epsilon/2}}{nq^2} \pm \sqrt{s^2 \frac{r^2 \omega_c^2 \epsilon}{2n^2 q^4} + \frac{v_A r \omega_c}{nq^2}}. \tag{38}$$

The above expression implies that for copropagation ($n > 0$), there is only one resonant velocity $v_r = v_r^+$ for all values of s. However, for counterpropagation ($n < 0$), both resonant velocities are possible if and only if $s > (q/r) \times (2|n|v_A R_0/\omega_c)^{1/2}$. For typical parameters of JET plasmas and for tornado modes with $n = [-4, -5, -6]$, this condition requires bounce harmonics satisfying $s > 4$.

1. Local theory: $\Delta_b^t \ll \Delta_m^{(i)}$

Similar to the case of passing particles, we find that the function G_m is determined mainly by the radial derivative of the inner mode structure at $r = r_m$. Using Eq. (36) and the equations for particle drift motion together with the resonance condition (37) for $s = 1$, we obtain

$$|G_m|^2 = \frac{v^4}{4\omega_c^2 R_0^2} \kappa^2 |\Phi_m^{(i)'}|^2 J_0^2(\xi). \tag{39}$$

Now substituting Eq. (39) into Eq. (11) and transforming the integration variable according to $d\lambda \simeq -2\epsilon d\kappa^2$, we arrive at the following expression for the growth rate:

$$\frac{\gamma}{\omega_r} = \frac{4\pi^3 \sqrt{2\epsilon} q M^2}{B_0^2 R_0} J_0^2(\xi) \frac{v_A v_r^6}{D_1}$$
$$\times \int_0^{\kappa_{max}^2} \kappa^2 d\kappa^2 \left[\left(1 - \frac{\omega_\star}{\omega_r}\right) \frac{\partial f_0}{\partial E} - \frac{\lambda}{E} \frac{\partial f_0}{\partial \lambda} \right], \tag{40}$$

where v_r is given by Eq. (38) and

$$D_1 = \frac{nqv_r}{rR_0\omega_c} + \frac{s}{qR_0} \sqrt{\frac{\epsilon}{2}}. \tag{41}$$

The above expressions take into account the effect of resonant interaction with the bounce motion and the toroidal precession motion of fast ions. The influence of the precessional drift frequency on the resonance condition can be neglected if $v_A/(\omega_c r_m) \ll \epsilon_m/(nq^2)$.

2. Nonlocal theory: $\Delta_m^{(i)} \ll \Delta_b^t \ll \Delta_m^{(o)}$

The function G_m is approximated as in the case of passing particles, i.e.,

$$G_m = \int_0^{\tau_b^t} \frac{dt}{\tau_b^t} \Phi_m^{(i)'}(r) v_D \sin \theta e^{-iS_0(0,t)}, \tag{42}$$

which for $s = 1$, gives

$$\int_{J_{\varphi1}}^{J_{\varphi2}} dJ_\varphi |G_m|^2 \left[\left(\frac{\omega_r}{\omega_\star} - 1\right) \frac{\partial f_0}{\partial J_\varphi} - \frac{\lambda}{E} \frac{\partial f_0}{\partial \lambda} \right]$$
$$\simeq \frac{C_m^2}{\Delta_m^{(i)}} \frac{2J_0^2(\xi) v_D^2 \kappa^2 \epsilon_m}{\pi^2 q} \int_{-D_t}^{D_t} dy \left[\left(\frac{\omega_r}{\omega_\star} - 1\right) \frac{\partial f_0}{\partial J_\varphi} - \frac{\lambda}{E} \frac{\partial f_0}{\partial \lambda} \right]$$
$$\times \left| \int_{-\pi/2}^{\pi/2} d\alpha \left[\frac{y + D_t \cos \alpha + 1/\alpha_m}{(y + D_t \cos \alpha)^2 + 1} e^{-i(\alpha + \pi/2)} \right. \right.$$
$$\left. \left. + \frac{y - D_t \cos \alpha + 1/\alpha_m}{(y - D_t \cos \alpha)^2 + 1} e^{i(\alpha + \pi/2)} \right] \sin \alpha e^{i\kappa \sin \alpha} \right|^2, \tag{43}$$

where $\Delta_b^t = 2(2/\epsilon_m)^{1/2} q \kappa v/\omega_c$ is the banana width at a given value of κ, and $D_t = \Delta_b^t/2\Delta_m^{(i)}$. Substituting Eq. (43) into Eq. (11), we obtain the following "nonlocal" expression for the TAE growth rate due to trapped particles:

$$\frac{\gamma}{\omega_r} = \frac{4\sqrt{2\epsilon} q M^2 v_A v_r^6}{B_0^2 R_0 D_1} J_0^2\left(\frac{mv_r}{r_m \omega_c}\right) \int_0^{\kappa_{max}^2} \kappa^2 d\kappa^2$$
$$\times \int_{-D_t}^{D_t} dy \left| \int_{-\pi/2}^{\pi/2} d\alpha \left[\frac{y + D_t \cos \alpha + 1/\alpha_m}{(y + D_t \cos \alpha)^2 + 1} e^{-i(\alpha + \pi/2)} \right. \right.$$
$$\left. \left. + \frac{y - D_t \cos \alpha + 1/\alpha_m}{(y - D_t \cos \alpha)^2 + 1} e^{i(\alpha + \pi/2)} \right] \sin \alpha e^{i\kappa \sin \alpha} \right|^2$$
$$\times \left[\left(1 - \frac{\omega_\star}{\omega_r}\right) \frac{\partial f_0}{\partial E} - \frac{\lambda}{E} \frac{\partial f_0}{\partial \lambda} \right], \tag{44}$$

where v_r is defined by Eq. (38).

3. Nonlocal theory: $\Delta_m^{(o)} \lesssim \Delta_b^t < r_m$

Taking into account the fact that the function G_m is determined mainly by the outer mode structure and using Eqs. (31), (36), and (37), we find from Eq. (11) for $s = 1$ resonance

$$\frac{\gamma}{\omega_r} = \frac{32\sqrt{2/\epsilon} q M^2 v_A v_r^6}{B_0^2 R_0 D_1} J_0^2\left(\frac{mv_r}{r_m \omega_c}\right) \int_0^{\kappa_{max}^2} \kappa^2 d\kappa^2 \frac{\Delta_m^{(i)}}{\Delta_b^t}$$
$$\times \frac{H(W^t)}{W^t} \left[\left(1 - \frac{\omega_\star}{\omega_r}\right) \frac{\partial f_0}{\partial E} - \frac{\lambda}{E} \frac{\partial f_0}{\partial \lambda} \right], \tag{45}$$

where $W^t = \Delta_b^t/2\Delta_m^{(o)}$, v_r is given by Eq. (38), and all quantities are calculated at $r = r_m$. The function $H(W^t)$ is defined as

$$H(W^t) = \frac{1}{4} \int_{-W^t}^{W^t} dy \left| \int_{-\pi/2}^{\pi/2} d\alpha [K_0(|y + W^t \cos \alpha|) e^{-i(\alpha + \pi/2)} \right.$$
$$\left. + K_0(|y - W^t \cos \alpha|) e^{i(\alpha + \pi/2)}] e^{i\kappa \sin \alpha} \right|^2. \tag{46}$$

The above integrals can be evaluated analytically by approximating $K_0 \simeq \pi \delta(y)$ to obtain $H(W^t) = 2\pi^2/W^t$ for $W^t \gg 1$ and $H(W^t) = 2\pi^2 W^t/3$ for $W^t \ll 1$.

The above set of expressions for the linear growth rate of TAEs, i.e., Eqs. (26), (32), (34), (40), (44), and (45), modify some prefactors of Ref. 24. Moreover, Eq. (32) has been kept in a less simplified form. However, the drive mechanism in the expressions is the same, and the remaining integrands
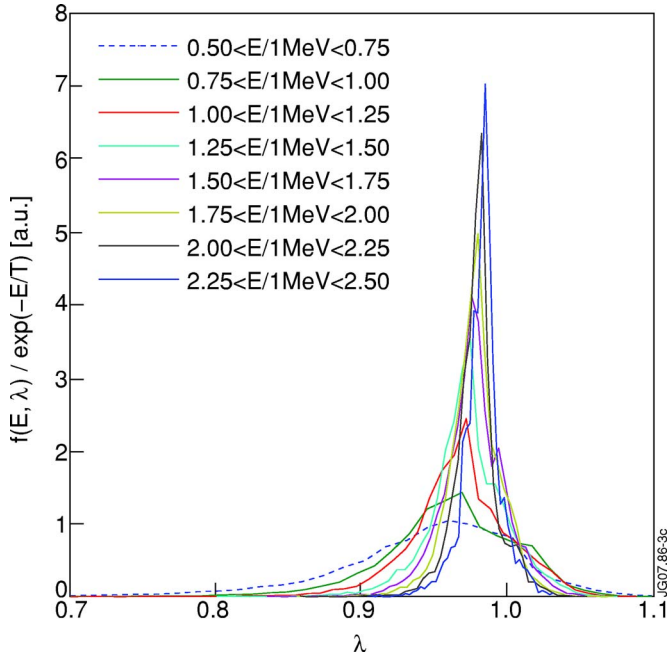
FIG. 12. (Color online) SELFO modeling output showing the hot ion velocity distribution function at different energies. The form of the hot ion velocity distribution function suggests an analytic model given by Eq. (47).

have been rewritten in order to obtain a condition for positive growth rate of bidirectional tornado modes, which is considered next.

C. Velocity anisotropy drive for tornado modes

We model the ICRH-accelerated protons with a velocity distribution function,[23]

$$f_0 = \alpha \bar{\beta} \exp(- E/T) \exp[- (\lambda - \langle\lambda\rangle)^2 / 2\sigma_\lambda^2], \tag{47}$$

strongly peaked in the pitch-angle variable around $\langle\lambda\rangle$. Here, σ_λ is the peaking parameter indicating the degree of anisotropy, T is the tail temperature, and α is a normalization constant chosen in such a way that

$$\bar{\beta} = \frac{8\pi}{B_0^2} \int_{-\pi}^{\pi} \frac{d\theta}{2\pi} \int d^3 p E f_0. \tag{48}$$

In order to analytically estimate the drive of bidirectional tornado modes, we start by rewriting Eq. (20) in order to obtain the velocity anisotropy criterion for driving tornado modes with negative toroidal mode numbers,

$$\sigma_\lambda^2 < \sigma_{\lambda,d}^2 = \left| \frac{T\lambda(\lambda - \langle\lambda\rangle)}{E\left(1 - \dfrac{\omega_\star}{\omega_r}\right)} \right|. \tag{49}$$

The form of the hot ion velocity distribution function in Eq. (47) is suggested by SELFO modeling.[27] Figure 12 illustrates modeled pitch-angle distribution functions of fast protons for JET shot No. 66203. The modeling shows that for energies $E \simeq 1$ MeV, the tail temperature is $T = 527$ keV, the pitch-angle center is $\langle\lambda\rangle = 0.96$, $d\bar{\beta}/dr = -0.12$, and $\bar{\beta} = 0.05$. From Eq. (49), we then find $\sigma_{\lambda,d} = [0.0509, 0.0551, 0.0594]$ for $n = [-6, -5, -4]$, where Eqs. (2) and (3) have been used in

order to obtain the values of the safety factor on the three different magnetic flux surfaces and the resonant frequencies $\omega_r = \omega_{TAE}$, respectively.

We note that the required change in σ_λ very nicely explains the experimental observation in Fig. 5 that counterpropagating tornado modes are delayed as compared to copropagating tornado modes, even though they are associated with the same magnetic flux surface and, hence, the eigenmode solutions appear simultaneously. However, the damping effect due to $d\bar{\beta}/dr$ is too high for counterpropagating tornadoes to be excited together with their corresponding copropagating tornadoes. As the value of $\sigma_\lambda \in [0.013, 0.065]$ drops below the critical value $\sigma_{\lambda,d}$, determined by Eq. (49), the velocity anisotropy drive for counterpropagating tornadoes becomes larger than the universal damping coming from a monotonic hot ion pressure profile. Since the limit for $n = -6$ is the most restrictive, it does not appear ahead of the $n = -5$ and $n = -4$ tornadoes, which would be the case otherwise.

For the parameters of JET shot No. 66203 at 20.2 s, we also find that the trapped particle orbit width satisfies $r_m > \Delta_b^t/2 \gg \Delta_m^{(o)}$. Hence, we are in the limit where the narrow banana width approximation, i.e., $r_m \gg \Delta_b^t/2$, is marginally satisfied for tornado modes with $n > 4$. Results from CASTOR-K modeling show that this is indeed the case.

V. CONCLUDING REMARKS AND DISCUSSION

Recent observations on JET have shown that bidirectional tornado modes can be excited by fast ions generated due to ICRH. In the present work the spectrum of bidirectional tornado modes is analyzed with a suite of MHD codes in order to determine the radial location, the toroidal mode numbers and the temporal evolution of the modes. Furthermore, the drive mechanism for bidirectional tornado modes both due to passing and trapped fast ions is investigated analytically and a condition for a positive instability growth rate, in terms of the parameters of the fast ion velocity distribution function, is derived and analyzed. It is found that the free energy coming from anisotropy of the fast ion velocity distribution function can strongly contribute to the mode excitation. For relevant plasma parameters, it is shown that the excitation condition is satisfied just before a giant sawtooth crash occurs. The results also explain why the counterpropagating tornado modes are excited simultaneously, whereas copropagating tornado modes are excited one-by-one. The reason is that, due to fast ion velocity space anisotropy, the TAE growth rate becomes positive in the case $n < 0$ for almost identical values of the peaking parameter that characterizes the degree of anisotropy.

Modeling by the CASTOR-K code indicates that the small banana width limit in the case of excitation by trapped fast ions is a good approximation for $n = +6$ tornado modes, and a reasonable approximation for $n = +5$ tornado modes. However, it is found that the excitation of $n = +4$ tornado modes is governed by potato-type orbits of the trapped fast ions. Since in our case, $r_{n=+6} > r_{n=+5} > r_{n=+4}$, this thus indicates that the tornado modes located radially further out have a smaller overlap with potato orbits and, instead, have a larger

overlap with banana orbits of trapped fast ions. In the near future, it is our intention to formulate a theory describing excitation of the TAEs by trapped fast ions having potato orbits. We also note that the analytical expressions for the TAE growth rate have been derived by applying a perturbative approach and the results should be verified by using numerical codes. Since at presence the CASTOR-K code can only be used for a growth rate calculation for the copropagating TAEs, an extension to the case of bidirectional TAEs would be required. Finally, we emphasize that in order to obtain realistic excitation conditions, the rates due to relevant damping mechanisms should be included in the analysis, which have been omitted in the present paper.

ACKNOWLEDGMENTS

[1] ITER Physics Basis 1999, Nucl. Fusion **39**, 2137 (1999).
[2] S. E. Sharapov, B. Alper, F. Andersson, Yu. F. Baranov, H. L. Berk, L. Bertalot, D. Borba, C. Boswell, B. N. Breizman, R. Buttery, C. D. Challis, M. de Baar, P. de Vries, L.-G. Eriksson, A. Fasoli, R. Galvao, V. Goloborod'ko, M. P. Gryaznevich, R. J. Hastie, N. C. Hawkes, P. Helander, V. G. Kiptily, G. J. Kramer, P. J. Lomas, J. Mailloux, M. J. Mantsinen, R. Martin, F. Nabais, M. F. Nave, R. Nazikian, J.-M. Noterdaeme, M. S. Pekker, S. D. Pinches, T. Pinfold, S. V. Popovichev, P. Sandquist, D. Stork, D. Testa, A. Tuccillo, I. Voitsekhovich, V. Yavorskij, N. P. Young, F. Zonca, JET-EFDA Contributors and the MAST Team, Nucl. Fusion **45**, 1168 (2005).
[3] D. Borba, B. Alper, R. V. Budny, A. Fasoli, R. F. Heeter, W. Kerner, S. E. Sharapov, and P. Smeulders, Nucl. Fusion **40**, 775 (2000).
[4] S. von Goeler, W. Stodiek, and N. Sauthoff, Phys. Rev. Lett. **33**, 1201 (1974).
[5] B. B. Kadomtsev, Sov. J. Plasma Phys. **1**, 389 (1976).
[6] D. Campbell, D. F. H. Start, J. A. Wesson, D. V. Bartlett, V. P. Bhatnagar, M. Bures, J. G. Cordey, G. A. Cottrell, P. A. Dupperex, A. W. Edwards, C. D. Challis, C. Gormezano, C. W. Gowers, R. S. Granetz, J. H. Hammen, T. Hellsten, J. Jacquinot, E. Lazzaro, P. J. Lomas, N. Lopes Cardozo, P. Mantica, J. A. Snipes, D. Stork, P. E. Stott, P. R. Thomas, E. Thompson, K. Thomsen, and G. Tonetti, Phys. Rev. Lett. **60**, 2148 (1988).
[7] F. Porcelli, Plasma Phys. Controlled Fusion **33**, 1601 (1991).
[8] F. Porcelli, Phys. Rev. Lett. **66**, 425 (1991).
[9] M. Saigusa, H. Kimura, Y. Kusama, G. J. Kramer, T. Ozeki, S. Moriyama, T. Oikawa, Y. Neyatani, and T. Kondoh, Plasma Phys. Controlled Fusion **40**, 1647 (1998).
[10] S. Bernabei, M. G. Bell, R. V. Budny, E. D. Fredrickson, N. N. Gorelenkov, J. C. Hosea, R. Majeski, E. Mazzucato, C. K. Phillips, G. Schilling, and J. R. Wilson, Phys. Rev. Lett. **84**, 1212 (2000).
[11] W. W. Heidbrink, E. D. Fredrickson, T. K. Mau, C. C. Petty, R. I. Pinsker, M. Porkolab, and B. W. Rice, Nucl. Fusion **39**, 1369 (1999).
[12] G. Y. Fu, Phys. Plasmas **2**, 1029 (1995).
[13] H. L. Berk, J. W. Van Dam, D. Borba, J. Candy, G. T. A. Huysmans, and S. Sharapov, Phys. Plasmas **2**, 3401 (1995).
[14] G. J. Kramer, S. E. Sharapov, R. Nazikian, N. N. Gorelenkov, and R. V. Budny, Phys. Rev. Lett. **92**, 015001 (2004).
[15] S. E. Sharapov, B. Alper, J. Fessey, N. C. Hawkes, N. P. Young, R. Nazikian, G. J. Kramer, D. N. Borba, S. Hacquin, E. de La Luna, S. D. Pinches, J. Rapp, D. Testa, and JET-EFDA Contributors, Phys. Rev. Lett. **93**, 165001 (2004).
[16] B. Alper, S. Hacquin, S. Sharapov, and JET/EFDA Team, Bull. Am. Phys. Soc. **50**, 226 (2005).
[17] S. E. Sharapov, in *Proceedings of the 21st International Conference on Fusion Energy 2006*, Chengdu (IAEA, Vienna, 2006), pp. EX/P6-19.
[18] S. Hacquin, B. Alper, S. Sharapov, D. Borba, C. Boswell, J. Fessey, L. Meneses, and M. Walsh, Nucl. Fusion **46**, S714 (2006).
[19] G. J. Kramer, C. Z. Cheng, Y. Kusama, R. Nazikian, S. Takeji, and K. Tobita, Nucl. Fusion **41**, 1135 (2001).
[20] C. Z. Cheng, L. Chen, and M. S. Chance, Ann. Phys. **161**, 21 (1985).
[21] G. Y. Fu and J. W. Van Dam, Phys. Fluids B **1**, 1949 (1989).
[22] B. N. Breizman and S. E. Sharapov, Plasma Phys. Controlled Fusion **37**, 1057 (1995).
[23] H. V. Wong and H. L. Berk, Phys. Lett. A **251**, 126 (1999).
[24] T. Fülöp, M. Lisak, Ya. I. Kolesnichenko, and D. Anderson, Plasma Phys. Controlled Fusion **38**, 811 (1996).
[25] B. N. Breizman, H. L. Berk, M. S. Pekker, S. D. Pinches, and S. E. Sharapov, Phys. Plasmas **10**, 3649 (2003).
[26] M. N. Rosenbluth and H. P. Rutherford, Phys. Rev. Lett. **34**, 1428 (1975).
[27] J. Hedin, T. Hellsten, L.-G. Eriksson, and T. Johnson, Nucl. Fusion **42**, 527 (2002).
[28] G. T. A. Huysmans, J. P. Goedbloed, and W. Kerner, *Proceedings of CP90 Conference on Computational Physics, Amsterdam* (World Scientific, Singapore, 1991), p. 371.
[29] S. Poedts and E. Schwartz, J. Comput. Phys. **105**, 165 (1993).
[30] A. B. Mikhailovskii, G. T. A. Huysmans, W. O. K. Kerner, and S. E. Sharapov, Plasma Phys. Rep. **23**, 844 (1997).
[31] S. E. Sharapov, A. B. Mikhailovskii, and G. T. A. Huysmans, Phys. Plasmas **11**, 2286 (2004).
[32] N. P. Young, S. E. Sharapov, and V. M. Nakariakov, Plasma Phys. Controlled Fusion **48**, 295 (2006).
[33] J. Candy, B. N. Breizman, J. W. Van Dam, and T. Ozeki, Phys. Lett. A **215**, 299 (1996).
[34] H. V. Wong, H. L. Berk, and B. N. Breizman, Nucl. Fusion **35**, 1721 (1995).
[35] H. L. Berk, B. N. Breizman, and H. Ye, Phys. Lett. A **162**, 475 (1992).
[36] D. Borba and W. Kerner, J. Comput. Phys. **153**, 101 (1999).